

Shape analysis and symmetry detection in gray-level objects using the analytical Fourier-Mellin representation

Stéphane Derrode^a and Faouzi Ghorbel^b

^a *Corresponding author,*

*Groupe Signaux Multi-dimensionnels, Institut Fresnel (UMR 6133),
École Nationale Supérieure de Physique de Marseille,
Domaine Universitaire de Saint Jérôme, 13013 Marseille Cedex 20, France.
Phone: int+ 33 4 91 28 28 49; Fax: int+ 33 4 91 28 88 13;
stephane.derrode@enspm.u-3mrs.fr*

^b *Groupe de Recherche Images et Formes de Tunisie, Laboratoire Cristal,
École Nationale des Sciences de l'Informatique,
Domaine Universitaire de La Manuba, 2010 Manuba, Tunisia.
Phone: int+ 216 1 600 444; Fax: int+ 216 1 600 449;
faouzi.ghorbel@ensi.rnu.tn*

Abstract

The analytical Fourier-Mellin transform is used in order to assess motion parameters between gray-level objects having the same shape with distinct scale and orientation. From results on commutative harmonic analysis, a functional is constructed in which the location of the minimum gives an estimation of the size and orientation parameters. Furthermore, when the set of geometrical transformations is restricted to the compact rotation group, we show that this minimum is exactly the Hausdorff distance between shapes represented in the Fourier-Mellin domain. This result is used for the detection and the estimation of both all rotation and reflection symmetric in objects.

Key words: Analytical Fourier-Mellin transform, Gray levels object, Scale and rotation parameters estimation, Hausdorff distance, Rotational and reflectional symmetries estimation.

Résumé

La transformée de Fourier-Mellin analytique est utilisée pour estimer les paramètres de mouvement entre des objets à niveaux de gris de même forme mais de taille et d'orientation différentes. À partir de résultats de l'analyse harmonique commutative, une fonctionnelle est construite pour laquelle le minimum fournit une estimation des paramètres d'échelle et d'orientation. De plus, lorsque l'on restreint l'ensemble des transformations géométriques au groupe compact des rotations, nous montrons que ce minimum est précisément la distance de Hausdorff entre formes lorsque ces dernières sont décrites dans le domaine de Fourier-Mellin. Ce résultat est utilisé pour la détection et la localisation de tous les axes de symétries par rotation et réflexion dans les objets.

Mots-clefs: Transformée de Fourier-Mellin analytique, Objets à niveaux de gris, Estimation des paramètres d'échelle et d'orientation, Distance de Hausdorff, Estimation des symétries par rotation et réflexion.

Number of pages: 23 + 3 (Biographical sketches + lists of figures and tables)

Number of tables: 1

Number of figures: 14

1 Introduction

The Mellin transform and the Fourier-Mellin transform (FMT) have been extensively studied for pattern description and recognition in the last decades. A number of works to date were motivated by the search for some sets of features invariant under rotation and scale [1, 2, 3]. Due to the crucial numerical problem faced in estimating the standard FMT [4], the analytical Fourier-Mellin transform (AFMT) was proposed in [5] and three efficient approximations were then presented [6]. In this work, we derive new algorithms for global motion parameters estimation, pattern matching and symmetry detection in gray-level objects using the AFMT.

The AFMT can be seen as the Fourier transform on the planar similarity group from the harmonic analysis viewpoint [7] and is well suited to extracting similarity invariant features. Extracting such a set of features needs the estimation of geometrical parameters to which the descriptors have to be invariant. The geometrical parameters correspond to the transformation that should be applied on a first object to recover the pose of the second one. In invariant pattern recognition, the estimation of the relative motion between two objects is generally done implicitly, i.e. hidden in the computation. For example, the normalization process proposed in [8] transforms an object back into a canonical form, i.e. the invariant representation of the object. Hence, the comparison between two objects is realized according to their canonical form.

This work is motivated by the same goals but with a different viewpoint. From results on commutative harmonic analysis for the group of similarities, a functional is constructed from the Euclidean distance between the AFMT representation of two objects. The location of its minimum allows to assess the scale and rotation parameters that should be applied on the first object to match the second. Furthermore, the correspondence problem is solved simultaneously according to the minimum value. The approach proposed needs neither invariant descriptors, nor matching primitives but works directly on gray-level objects. It is related to global image registration methods designed for the similarity group such as correlation and matching filters [9, 10, 11, 12].

Another interesting application of the method concerns the detection and localization of symmetry axes in gray-level images. Indeed, when the set of geometrical transformations is restricted to the compact rotation group, we show that the minimum of the functional is precisely the Hausdorff distance between shapes when expressed in the Fourier-Mellin domain. Hence, two algorithms are derived in order to estimate all the rotational- and reflectional-symmetric axes of any gray-level object. The method is related to some extent to the work proposed in [13], in the case of reflectional symmetry, where the

authors minimize an energy function constructed from the complex moments of images.

This paper is organized as follows. The AFMT and some of its relevant properties are presented in section 2. In particular, we give the appropriate Parseval equality and shift theorem and we define precisely the notion of shape according to the planar similarity group. Based on these properties, section 3 presents a method for estimating the rotation and scale factor parameters by using a functional constructed from the AFMT representation of objects. When the transformation group is restricted to pure rotation, we then show that the minimum of the functional is precisely the Hausdorff distance expressed in the Fourier-Mellin domain. From the last result, we derive in section 4 two algorithms for the detection and localization of both all rotational and reflectional symmetries of an image. All the algorithms are illustrated with experiments on both synthetic and real gray-level images.

2 Formulation and notation

The aim of this section is to sketch some theoretical results and useful properties concerning group theory and commutative harmonic analysis for the direct similarity group in order to set a rigorous background for planar gray-level shape analysis. Further results and applications on commutative harmonic analysis in the image processing field can be found in [7, 14, 15] for example.

Throughout this paper, we shall denote by \mathbb{Z} the additive group of integers, \mathbb{R} the additive group of the real line, \mathbb{R}_+^* the multiplicative group of positive and non-zero real numbers and \mathbb{S}^1 the unit circle of the plane \mathbb{R}^2 . All these groups are locally compact and commutative. The direct product $\mathcal{G} = \mathbb{R}_+^* \times \mathbb{S}^1$ forms a locally compact and commutative group under the following law : $(\alpha, \theta) \circ (\rho, \psi) = (\alpha\rho, \theta + \psi)$. \mathcal{G} is formed by all planar and positive similarities centered on the origin of axes and is equivalent to the polar coordinate space.

2.1 The analytical Fourier-Mellin transform

We denote by $\mathbf{L}^p(\mathcal{G})$ the normed vector spaces of integrable ($p = 1$) and square integrable ($p = 2$) real valued functions defined on \mathcal{G} :

$$f \in \mathbf{L}^p(\mathcal{G}) \Leftrightarrow \|f\|_{\mathbf{L}^p(\mathcal{G})} = \left(\int_0^\infty \int_0^{2\pi} |f(r, \theta)|^p d\theta \frac{dr}{r} \right)^{\frac{1}{p}} < \infty, \quad (1)$$

where $r^{-1}dr d\theta$ is a positive and invariant measure on \mathcal{G} (the Haar measure [16]).

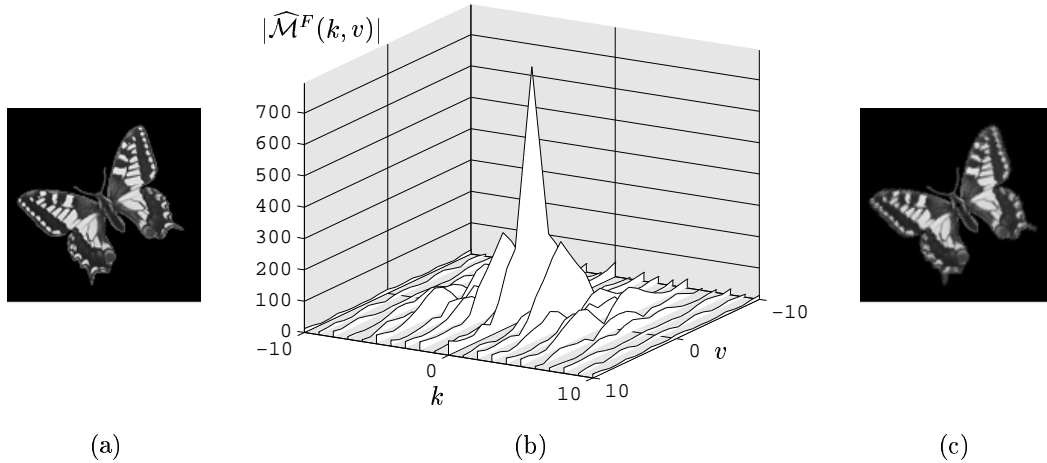


Fig. 1. Direct and inverse AFMT approximations (fast algorithm, $\sigma = 0.5$). (a) Original image. (b) Magnitude of central Fourier-Mellin harmonics. (c) Reconstructed version from a finite and discrete Fourier-Mellin spectrum.

The Fourier-Mellin Transform (FMT) is defined for functions in $\mathbf{L}^1(\mathcal{G})$. However, in general, gray-scale images cannot be assimilated to such functions and it was proposed to compute the FMT of $f_\sigma(r, \theta) = r^\sigma f(r, \theta)$ with $\sigma > 0$ [5]. Since any real image f is bounded, f_σ belongs to $\mathbf{L}^1(\mathcal{G})$. Using harmonic analysis results, it is easy to show that the dual group of \mathcal{G} is $\hat{\mathcal{G}} = \mathbb{Z} \times \mathbb{R}$ [16], which represent the parameters space in the Fourier-Mellin domain. The FMT of f_σ is called the Analytical Fourier-Mellin Transform (AFMT) of f and can be written in this way:

$$\forall(k, v) \in \hat{\mathcal{G}}, \quad \mathcal{M}_{f_\sigma}(k, v) = \frac{1}{2\pi} \int_0^\infty \int_0^{2\pi} f(r, \theta) r^{\sigma-iv} e^{-ik\theta} d\theta \frac{dr}{r}. \quad (2)$$

Hence, the AFMT can be seen as the Laplace transform on the planar similarity group.

The AFMT gives a unique description and images can be retrieved with the inverse transform. Recently, three approximations of the AFMT, i.e. direct, fast and Cartesian estimations, were proposed and used for the reconstruction of images from a finite and discrete set of harmonics [6]. These approximations differ in the re-sampling of images into polar, log-polar and Cartesian coordinates and in the way numerical integration is performed. It was found that the fast algorithm performs better, in the \mathbf{L}^2 -reconstruction error sense, than the other two approximations. The fast algorithm involves re-sampling the Cartesian image according to a log-polar grid and computing the AFMT integrals with a two dimensional FFT. Conversely, the original image is reconstructed from a 2D inverse FFT and log-polar to Cartesian re-sampling. Fig. 1 illustrates a reconstruction result obtained from the fast algorithm.

2.2 Parseval equality for the similarity group

We denote by $\mathbf{L}^2(\hat{\mathcal{G}})$, the normed vector space of square integrable complex valued functions defined on $\hat{\mathcal{G}}$:

$$h \in \mathbf{L}^2(\hat{\mathcal{G}}) \Leftrightarrow \|h\|_{\mathbf{L}^2(\hat{\mathcal{G}})} = \left(\int_{-\infty}^{+\infty} \sum_{k \in \mathbb{Z}} |h(k, v)|^2 dv \right)^{\frac{1}{2}} < \infty. \quad (3)$$

The Plancherel theorem can be extended to every locally compact and commutative group [17]. For f_σ in $\mathbf{L}^1(\mathcal{G}) \cap \mathbf{L}^2(\mathcal{G})$, $\mathcal{M}_{f_\sigma} \in \mathbf{L}^2(\hat{\mathcal{G}})$ and the Parseval equality is given by :

$$\|f_\sigma\|_{\mathbf{L}^2(\mathcal{G})} = \|\mathcal{M}_{f_\sigma}\|_{\mathbf{L}^2(\hat{\mathcal{G}})}, \quad (4)$$

$$\int_0^\infty \int_0^{2\pi} r^{2\sigma} |f(r, \theta)|^2 d\theta \frac{dr}{r} = \int_{-\infty}^{+\infty} \sum_{k \in \mathbb{Z}} |\mathcal{M}_{f_\sigma}(k, v)|^2 dv.$$

In what follows, we assume that a gray-level object is represented by a function $f_\sigma \in \mathbf{L}^1(\mathcal{G}) \cap \mathbf{L}^2(\mathcal{G})$ (original description) or, in a strictly equivalent way, by its FMT $\mathcal{M}_{f_\sigma} \in \mathbf{L}^2(\hat{\mathcal{G}})$ (dual Fourier-Mellin description).

2.3 Gray-level shape and shift theorem for planar similarities

The intuitive notion of the *shape of an object* has been defined rigorously by several authors [18, 14, 7, 19]. An object retains its shape whatever its position in the image. So, the notion of shape is directly connected to a group of transformations. In the case of gray-level shapes and similarity transformations, shapes can be characterized efficiently by the AFMT using an appropriate shift theorem. The following is inspired by the results obtained in the case of planar contours and Fourier descriptors [20].

Let f^2 denote the rotation and size change of an object f^1 through angle $\beta \in \mathbb{S}^1$ and scale factor $\alpha \in \mathbb{R}_+^*$, i.e. $f^2(r, \theta) = f^1(\alpha r, \theta + \beta)$. Two such objects will be termed similar objects. It is easy to show that their AFMT are related according to:

$$\forall (k, v) \in \hat{\mathcal{G}}, \quad \mathcal{M}_{f_\sigma^2}(k, v) = \alpha^{-\sigma+iv} e^{ik\beta} \mathcal{M}_{f_\sigma^1}(k, v). \quad (5)$$

These relations can be seen as the shift theorem for the planar and positive similarity group. The AFMT converts a similarity transformation in the original domain into a complex multiplication in the Fourier-Mellin domain. This makes the AFMT appropriate for the extraction of descriptors invariant to

object changes in scale and orientation and a complete family of similarity invariant descriptors has been designed [5]. In the following, we intend to show how the shift theorem can be used to estimate the two geometrical parameters.

Going through the group of positive similarities, the shape \mathbb{F} of an object f could be defined as the set of all similar objects according to \mathcal{G} :

$$\mathbb{F} = \left\{ \left(f(\alpha r, \theta + \beta) \right)_{(r, \theta) \in \mathcal{G}}, (\alpha, \beta) \in \mathbb{R}_+^* \times \mathbb{S}^1 \right\}, f_\sigma \in \mathbf{L}^1(\mathcal{G}) \cap \mathbf{L}^2(\mathcal{G}), \quad (6)$$

and, using Eq. (4) and (5), a shape is also defined in a strictly equivalent way in the Fourier-Mellin domain by:

$$\mathbb{F} = \left\{ \left(\alpha^{-\sigma+iv} e^{ik\beta} \mathcal{M}_{f_\sigma}(k, v) \right)_{(k, v) \in \hat{\mathcal{G}}}, (\alpha, \beta) \in \mathbb{R}_+^* \times \mathbb{S}^1 \right\}, \mathcal{M}_{f_\sigma} \in \mathbf{L}^2(\hat{\mathcal{G}}). \quad (7)$$

It can be shown that a shape is an equivalence class through the action of \mathcal{G} [21, 7]. It is important to note that such a class is not compact since \mathbb{R}_+^* is not.

Every object f can be considered as a representative of its shape \mathbb{F} . An object f^i in \mathbb{F} is related to f by a similarity transformation $(\alpha_i, \beta_i) \in \mathbb{S}^1$, i.e. $f^i(r, \theta) = f(\alpha_i r, \theta + \beta_i)$, or $\mathcal{M}_{f_\sigma^i}(k, v) = \alpha_i^{-\sigma+iv} e^{ik\beta_i} \mathcal{M}_{f_\sigma}(k, v)$. Of course, the converse also applies with parameters $\alpha = \frac{1}{\alpha_i}$ and $\beta = -\beta_i$. In this context, the assessment of parameters between two similar objects involves finding their relative position inside a shape. One important point is to determine beforehand whether the objects belong to the same shape or not.

3 Accurate estimation of scale and rotation parameters

In this section, we intend to derive a new algorithm dedicated to the estimation of size and orientation differences between two objects from their AFMT representation. The method is based on the computation of the Euclidean distance between objects expressed in the Fourier-Mellin domain, by using the Plancherel (4) and shift (5) theorems. Experiments are conducted on the three images of butterflies shown in figure 2, with the fast approximation of the AFMT [6]. We start with a straightforward algorithm that will serve later, and finish with an interesting result regarding the special case of the one parameter compact group of rotations.

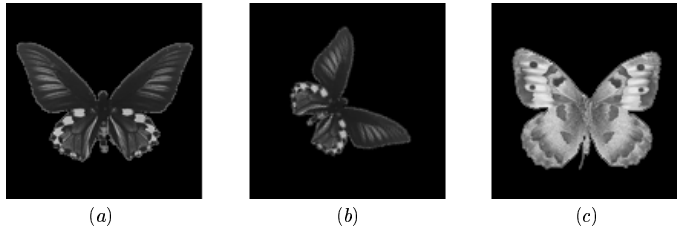


Fig. 2. Three images of a butterfly used for the illustration of algorithms. Images (a) and (b) represent the same butterfly with distinct positions ($\alpha = 0.75$ and $\beta = 60^\circ$). The (b) picture has been artificially computed from the (a) one. Image (c) is a butterfly with a distinct shape.

3.1 An elementary algorithm

One straightforward way to estimate parameters between two similar objects f^1 and f^2 can be derived directly from the shift theorem. Taking the modulus and phase of both sides of Eq. (5) leads to the explicit expression of the parameters:

$$\begin{cases} \alpha = \left| \frac{\mathcal{M}_{f_\sigma^1}(k, v)}{\mathcal{M}_{f_\sigma^2}(k, v)} \right|^{\frac{1}{\sigma}} \\ \beta = \frac{1}{k} \left(\arg \mathcal{M}_{f_\sigma^2}(k, v) - \arg \mathcal{M}_{f_\sigma^1}(k, v) - v \ln \alpha \right) \text{ mod } \left(\frac{2\pi}{k} \right) \end{cases} \quad (8)$$

for k , $\mathcal{M}_{f_\sigma^1}(k, v)$ and $\mathcal{M}_{f_\sigma^2}(k, v)$ non zero.

Under these assumptions, every AFMT harmonic can be used to estimate the geometrical parameters. This algorithm has been used in [22], with $v = 0$. A similar method has also been designed in the case of geometric moments and the estimation of affine motion [23]. In this work, the affine parameters between two objects are estimated with six moments up to order three.

Although very quick, this kind of algorithm suffers from the following major drawbacks:

- (1) The algorithm supposes the two objects have the same shape and the matching task is assumed to have been done previously.
- (2) The estimation $\hat{\beta}$ depends on the estimation $\hat{\alpha}$ so that errors are cumulated. Furthermore, due to the $\frac{1}{k}$ term in the expression of β , a phase wrapping problem occurs.
- (3) Different couples (k_i, v_i) may produce several estimations $\hat{\alpha}_i$ and $\hat{\beta}_i$, since we only get an approximation of Fourier-Mellin harmonics. The reliability of the estimation depends on the choice of the harmonics. One solution is to compute the mean of several estimations, but the second point remains.

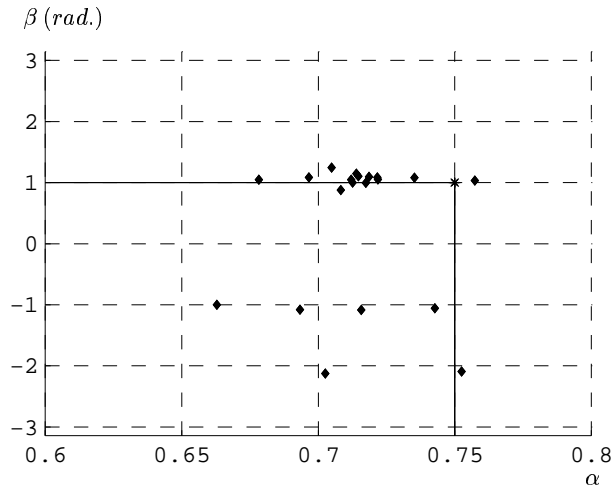


Fig. 3. Illustration of the elementary algorithm using images (a) and (b) in Fig. 2. The cross symbol denotes the real parameters ($\alpha = 0.75$, $\beta = 1$ rad) whereas a diamond shows an estimate.

The last two points are illustrated in Fig. 3 where different estimates of the parameters between the two similar objects in Fig. 2 are reported. We used about 20 couples (k_i, v_i) within the range $[-5, 5] \times [-5, 5]$. The scale factor is often underevaluated by 5 to 10% while the rotation angle can appear far from the expected value, mainly due to the phase wrapping problem (2). One important practical point is that the accuracy of estimations is more reliable when relatively small order Fourier-Mellin harmonics are involved in the computation.

3.2 AFMT-based Euclidean matching algorithm

A rigorous solution is now presented, based on the results in section 2. The algorithm described below can both detect whether two objects have the same shape and estimate their relative position.

The Euclidean norm in Eq. (1) can be used to compare two objects f and g by computing $\|f_\sigma - g_\sigma\|_{\mathbf{L}^2(\mathcal{G})}$. It is zero if and only if the objects are strictly identical and cannot be used to compare objects of different size and orientation. To take into account possible changes in orientation and size, we formulate the problem as follows: for all (ρ, ψ) in $\mathbb{R}_+^* \times \mathbb{S}^1$, we define the functional \mathbf{E} according to:

$$\mathbf{E}_{f_\sigma, g_\sigma}(\rho, \psi) = \|f_\sigma(r, \theta) - g_\sigma(\rho r, \theta + \psi)\|_{\mathbf{L}^2(\mathcal{G})}. \quad (9)$$

By using the Parseval equality (4) and the shift theorem for g_σ (5), \mathbf{E} can be rewritten with the appropriate norm in the Fourier-Mellin domain: $\forall(\rho, \psi) \in$

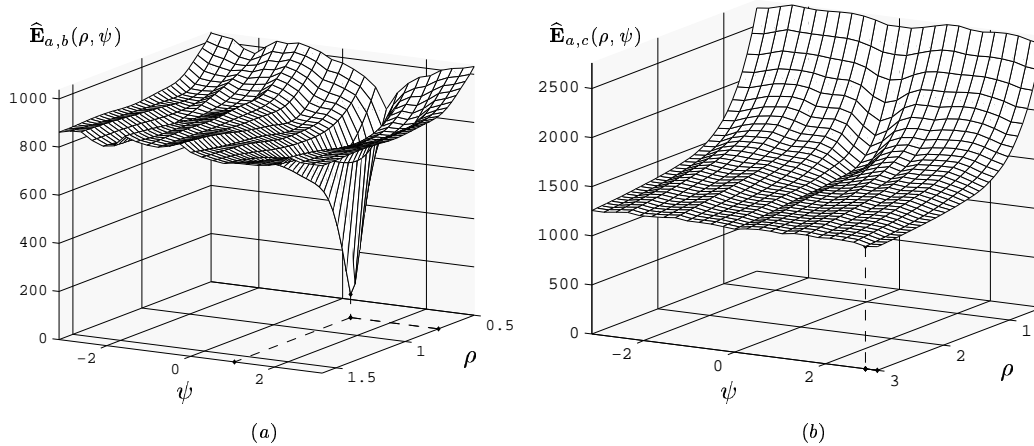


Fig. 4. Three-dimensional plots of \mathbf{E} for (a) the similar images, and (b) the distinct images in Fig. 2. Figure (b) clearly shows no prevailing minimum.

$$\mathbb{R}_+^* \times \mathbb{S}^1,$$

$$\begin{aligned} \mathbf{E}_{f_\sigma, g_\sigma}(\rho, \psi) &= \left\| \mathcal{M}_{f_\sigma(r, \theta)} - \mathcal{M}_{g_\sigma(\rho r, \theta + \psi)} \right\|_{\mathbf{L}^2(\hat{\mathcal{G}})}, \\ &= \left(\int_{-\infty}^{+\infty} \sum_{k \in \mathbb{Z}} \left| \mathcal{M}_{f_\sigma}(k, v) - \rho^{-\sigma + iv} e^{ik\psi} \mathcal{M}_{g_\sigma}(k, v) \right|^2 dv \right)^{\frac{1}{2}}. \end{aligned} \quad (10)$$

When parameters ρ and ψ go through the similarity group, we get a measure of the objects' correspondance for each location of the transformation group. If $\mathbf{E} = 0$ for a certain couple (α, β) , then the matching between the objects is achieved (the objects should be considered as similar) and the parameters (α, β) correspond to the similarity transformation that should be applied on the first object to match the second. Note that the couple of parameters is not necessarily unique, e.g. rotationally symmetric images, see section 4.

3.3 Algorithm efficiency, optimization and experimental results

The computation of \mathbf{E} in the Fourier-Mellin domain (10) is much more efficient and reliable than the direct computation in the original shape space (9). Indeed, rotation and scale transformations are not suited to the Cartesian grid and interpolation between gray-levels is necessary for each polar coordinates $(\rho r, \theta + \psi)$. This can be an important source of numerical error. On the other hand, the computation from (10) needs only complex multiplications, without additional error and the complexity is greatly reduced. Furthermore, this formulation makes it possible to use a discrete and finite extent set of AFMT harmonics.

Figure 4 shows a 3D representation of the matching functions obtained from the AFMT representations of the butterfly images in Fig. 2. The spectrum sizes were set to $k \in [-20; 20]$ and $v \in [-20; 20]$, that is to say 1681 harmonics for each image. The surface exhibits a well-pronounced pit for similar objects with a minimum value located at the expected parameters (a). Such a pit cannot be found in the case of the two distinct objects (b). In this case, it should also be pointed out that the surface decreases more and more slowly as the scale parameter increases and the rotation angle has almost no influence on the measure.

Due to approximations and the anisotropy of the Cartesian grid to similarity transformations, the minimum value is not exactly zero for similar objects and the estimation of motion parameters becomes the search for a couple $(\hat{\rho}_{\mathbf{E}}, \hat{\psi}_{\mathbf{E}})$ which minimizes the functional (10):

$$(\hat{\rho}_{\mathbf{E}}, \hat{\psi}_{\mathbf{E}}) = \arg \left(\underbrace{\min_{\rho \in \mathbb{R}_+^*, \psi \in \mathbb{S}^1} \hat{\mathbf{E}}_{f_{\sigma}, g_{\sigma}}(\rho, \psi)}_{\hat{\mathbf{E}}_{f_{\sigma}, g_{\sigma}}^{\min}} \right). \quad (11)$$

The location of the minimum value is estimated using a classical optimization algorithm based on a modification of Powell's algorithm [24]. The method does not need derivatives and the descent along the gradient is reiterated until convergence is attained, according to a given threshold. This algorithm is known to be quite simple but sensitive to the presence of local optima. Therefore, the choice for a convenient initial value is of importance. We used the estimation provided by the elementary algorithm described in section 3.1, computed from the harmonic defined by $(k = 1, v = 1)$. When the optimization process does not converge to values within reasonable limits (given by the image borders), we may conclude that the objects have distinct shapes and the estimation of parameters is not required.

The optimization process is illustrated in Fig. 5 for the butterfly images (a) and (b) in Fig. 2. The 3D surface shows a zoom on the pit of figure 4(a). The smoothness of the surface on the small scale is mainly due to the robustness of the AFMT approximation algorithm.

The five steps toward the optimization process are reported in table 1. The initial values obtained from the elementary algorithm are $\hat{\rho}_0 = 0.6832$, $\hat{\psi}_0 = 59.63^\circ$ and $\hat{\mathbf{E}}_{a,b}^0 = 313.21$. The final estimation was obtained after 5 iterations. We get the following values : $\hat{\rho}_{\mathbf{E}} = 0.7489$, $\hat{\psi}_{\mathbf{E}} = 59.95^\circ$ and $\hat{\mathbf{E}}_{a,b}^{\min} = 85.63$. One interesting point is the great improvement for the estimation of the scale parameter: the error reduces from 8.9% to 0.15%. The minimum value is also divided by a factor of 3.7.

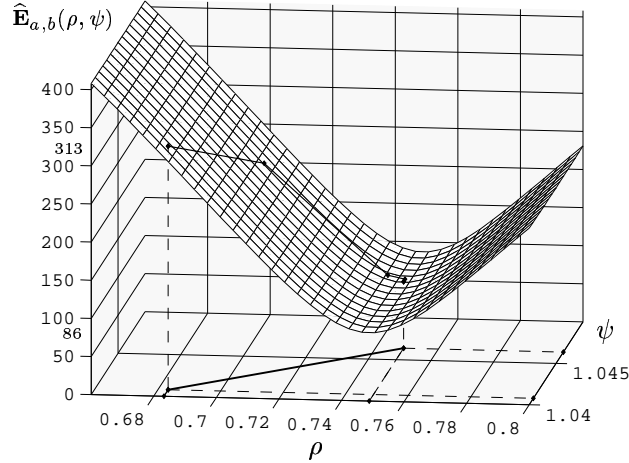


Fig. 5. Zoom on the pit in figure 4(a). The path through the surface shows the five optimization steps from the initial estimation $(\hat{\rho}_0, \hat{\psi}_0)$ to the final estimation $(\hat{\rho}_{\mathbf{E}}, \hat{\psi}_{\mathbf{E}})$ (cf. Table 1). The threshold has been set to 10^{-5} .

Table 1

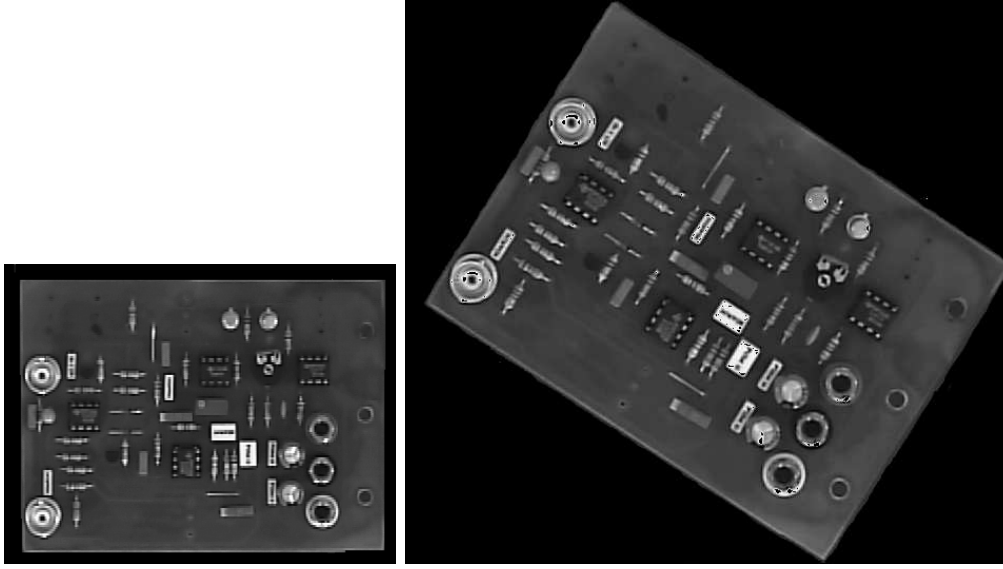
Optimization steps for images (a) and (b) in Fig. 2.

Iteration (i)	$\hat{\rho}_i$	$\hat{\psi}_i$	$\hat{\mathbf{E}}_{a,b}^i$
0	0.6832	1.0408 (59.63°)	313.21
1	0.7032	1.0470 (59.99°)	227.03
2	0.7432	1.0468 (59.98°)	89.34
3	0.7488	1.0467 (59.97°)	85.64
4	0.7489	1.0464(59.95°)	85.63

A second estimation result is reported in Fig. 6. Two pictures of an electronic board lying on a nearly uniform background were acquired with a digital camera. The change of pose was obtained by performing a camera zoom and a rotation of the board. The pit in Fig. (c) is less sharp than the one in Fig. 4 but is still well pronounced. We obtained the following estimates after six iterations : $\hat{\rho}_6 = 0.76$, $\hat{\psi}_6 = -0.61$ (34.7°) and $\hat{\mathbf{E}}_{a,b}^6 = 221.5$. We verified that these parameters correspond to the similarity transform that should be applied on the (b) image to match the (a) one.

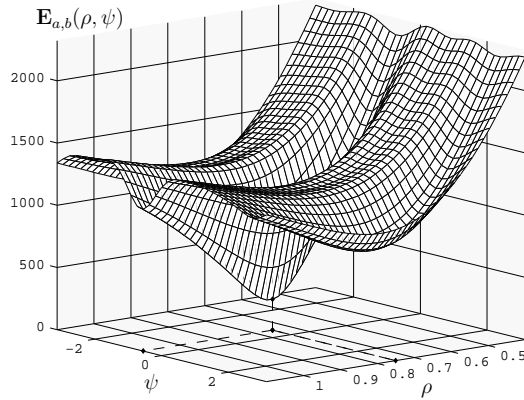
3.4 Plane rotation group and Hausdorff distance between shapes

When the group of transformations is restricted to the compact group of rotations, we now show that the minimum of \mathbf{E} is precisely the Hausdorff distance between shapes when expressed in the AFMT domain. For pattern matching, the Hausdorff distance has mainly been used for comparing point sets and



(a)

(b)



(c)

Fig. 6. Two still pictures of an electronic board acquired with a digital camera. The (c) image represents the three-dimensional plot of \mathbf{E} and exhibits a minimum that corresponds to the estimated scale and rotation parameters between (a) and (b).

straight lines between an image and a pattern [25, 26, 27].

If the set of transformations is restricted to the one parameter plane rotation group \mathbb{S}^1 , a shape is formed by all similar objects up to a rotation. In the Fourier-Mellin domain, we get from Eq. (7) (setting $\alpha = 1$):

$$\mathbb{F} = \left\{ \left(e^{ik\beta} \mathcal{M}_{f_\sigma}(k, v) \right)_{(k,v) \in \hat{\mathcal{G}}}, \beta \in \mathbb{S}^1 \right\}, \quad \mathcal{M}_{f_\sigma} \in \mathbf{L}^2(\hat{\mathcal{G}}).$$

The restriction of \mathbf{E} in Eq. (10) to \mathbb{S}^1 is then:

$$\mathbf{E}_{f_\sigma, g_\sigma}(\psi) = \left(\int_{-\infty}^{+\infty} \sum_{k \in \mathbb{Z}} \left| \mathcal{M}_{f_\sigma}(k, v) - e^{ik\psi} \mathcal{M}_{g_\sigma}(k, v) \right|^2 dv \right)^{\frac{1}{2}}. \quad (12)$$

Shapes are now compact and bounded sets since there exists a continuous bijection with \mathbb{S}^1 . The shape space becomes the quotient space $\mathbf{L}^2(\mathbb{Z} \times \mathbb{R})/\mathbb{S}^1$ which is a metric space with the Hausdorff distance [16, 7]. We now extend the result obtained on closed contours and Fourier coefficients [20] to gray-level images and AFMT.

The Hausdorff distance between two shapes \mathbb{F} and \mathbb{G} is given by:

$$\Delta(\mathbb{F}, \mathbb{G}) = \max(\delta(\mathbb{F}, \mathbb{G}), \delta(\mathbb{G}, \mathbb{F})),$$

in which $\delta(\mathbb{F}, \mathbb{G}) = \max_{f \in \mathbb{F}} \min_{g \in \mathbb{G}} d_2(f, g)$ and d_2 is the Euclidean distance derived from the \mathbf{L}^2 -norms. In the Fourier-Mellin domain, the Hausdorff distance can be written:

$$\begin{aligned} \delta(\mathbb{F}, \mathbb{G}) &= \max_{\varphi \in \mathbb{S}^1} \min_{\phi \in \mathbb{S}^1} \left\| e^{ik\varphi} \mathcal{M}_{f_\sigma}(k, v) - e^{ik\phi} \mathcal{M}_{g_\sigma}(k, v) \right\|_{\mathbf{L}^2(\hat{\mathcal{G}})}, \\ &= \max_{\varphi \in \mathbb{S}^1} \min_{\phi \in \mathbb{S}^1} \left\| \mathcal{M}_{f_\sigma}(k, v) - e^{ik(\phi-\varphi)} \mathcal{M}_{g_\sigma}(k, v) \right\|_{\mathbf{L}^2(\hat{\mathcal{G}})}. \end{aligned}$$

Using the following change of variable $\psi = \phi - \varphi$, we get:

$$\begin{aligned} \delta(\mathbb{F}, \mathbb{G}) &= \min_{\psi \in \mathbb{S}^1} \left\| \mathcal{M}_{f_\sigma}(k, v) - e^{ik\psi} \mathcal{M}_{g_\sigma}(k, v) \right\|_{\mathbf{L}^2(\hat{\mathcal{G}})}, \\ &= \min_{\psi \in \mathbb{S}^1} \mathbf{E}_{f_\sigma, g_\sigma}(\psi), \end{aligned}$$

since parameter φ no longer exists.

In a similar way, we also get:

$$\delta(\mathbb{G}, \mathbb{F}) = \min_{\psi \in \mathbb{S}^1} \mathbf{E}_{g_\sigma, f_\sigma}(\psi) = \min_{\psi \in \mathbb{S}^1} \mathbf{E}_{f_\sigma, g_\sigma}(\psi),$$

and the Hausdorff distance is reduced to the following quantity :

$$\Delta(\mathbb{F}, \mathbb{G}) = \min_{\psi \in \mathbb{S}^1} \mathbf{E}_{f_\sigma, g_\sigma}(\psi). \quad (13)$$

Hence, the minimum value of \mathbf{E} in Eq. (12) is exactly the Hausdorff distance between shapes. This result ensures the uniqueness of parameters and is the basis for the symmetry detection algorithms presented in the next section.

For illustration purposes, figure 7 shows the Hausdorff distance (b) computed from the two images in (a). The minimum value is attained for $\psi = 35^\circ$ which is precisely the orientation difference between the two images.

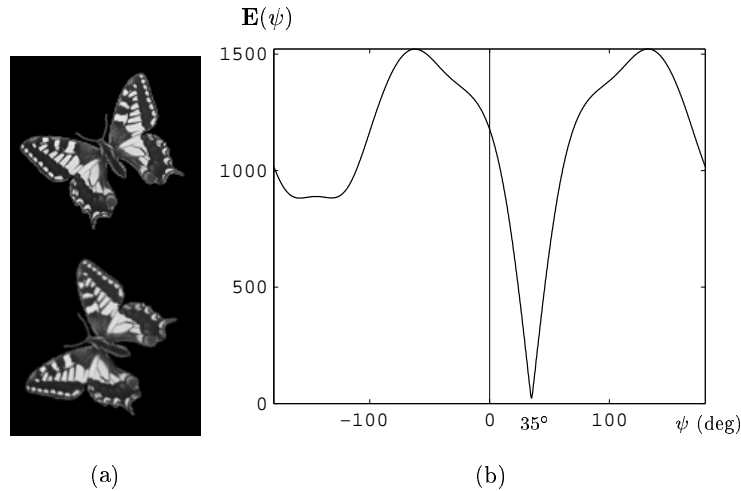


Fig. 7. Plot of the Hausdorff distance (b) computed from the two images in (a). The second picture has been artificially computed from the first one. The minimum value $\Delta = 23.61$ is attained for $\psi = 35.02^\circ$.

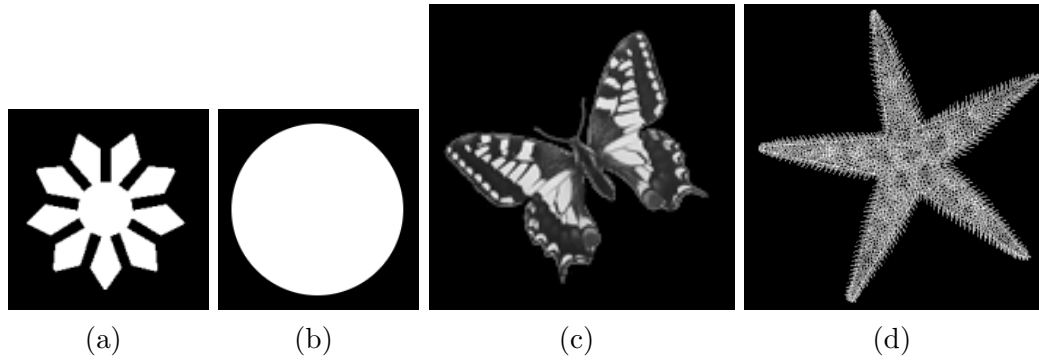


Fig. 8. Four test images used for symmetry detection and estimation experiments. (a) and (b) are binary images whereas (c) and (d) are gray-level ones.

4 Rotation and reflection symmetry estimation

Two algorithms are now derived for the detection and estimation of both rotational and reflectional symmetries in gray-level images. For algorithm illustration purposes, experiments are conducted on the four test images in Fig. 8. Image (a) shows nine rotation and reflection symmetries. The image in (b) represents a special case of an image with an "infinite number" of symmetry. The butterfly (c) presents one reflection and no rotation symmetry whereas the starfish (d) shows five prevailing axes of both symmetry types. We finish with some symmetry detection results obtained from real gray-level images of aerial images of roundabouts.

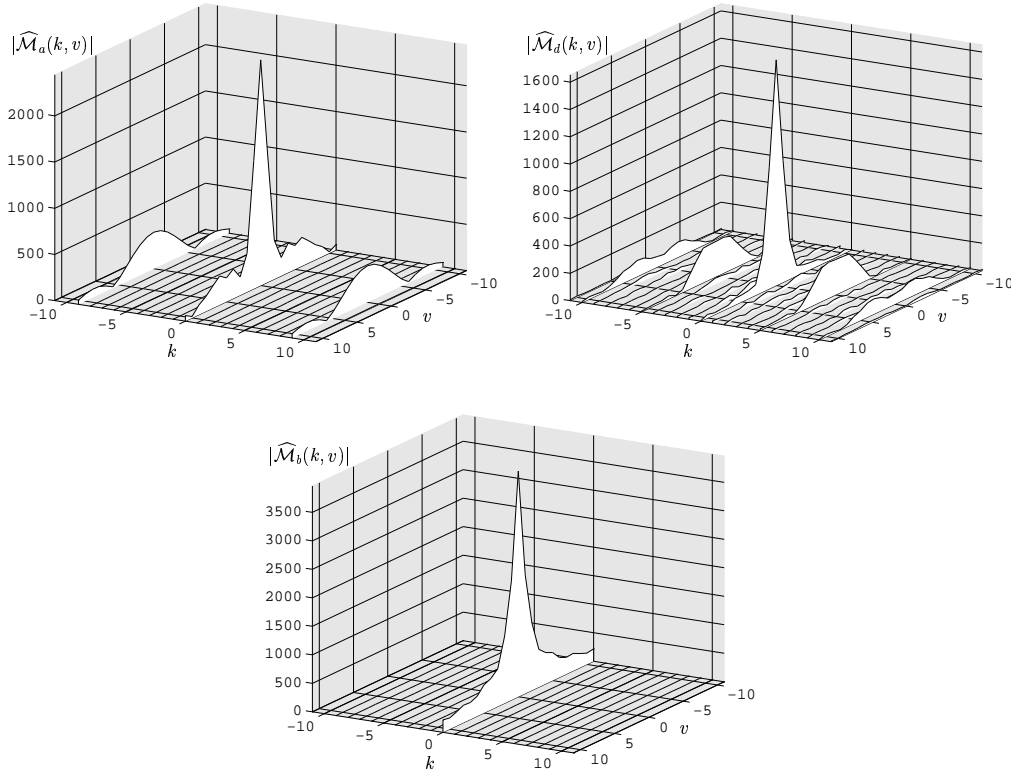


Fig. 9. Magnitude of central Fourier-Mellin harmonics of the images (a), (d) and (b) in Fig. 8, respectively.

4.1 Rotationally symmetric images

In this paragraph, we use the Hausdorff distance for the detection and the estimation of folds in rotationally symmetric images. Following [28], a 2D image is called P rotationally symmetric (P-RSI for short), if it is invariant under rotation of $2\pi/P$ about the center of gravity of the object and P is the largest integer:

$$\forall (r, \theta) \in \mathbb{R}_+^* \times \mathbb{S}^1, \quad f(r, \theta) = f\left(r, \theta + \frac{2\pi l}{P}\right), \quad l = 0, \dots, P-1. \quad (14)$$

The AFMT can be seen as the analytical Mellin transform of the Fourier coefficients of an image. Since the Fourier coefficients $\mathcal{F}(k)$ of a P-RSI f is zero for every k not a multiple of P , the AFMT is zero except for k multiple of P and v real. This is illustrated in Fig. 9 which shows the magnitude of central Fourier-Mellin harmonics of the three rotationally symmetric images in Fig. 8. In the first two cases, the AFMT is approximately zero for k a multiple of nine and five respectively, which corresponds to the number of fold axes in the images. In the case of the disk, the Fourier-Mellin transform is zero except for $k = 0$ and corresponds to the special case of an image with an "infinite

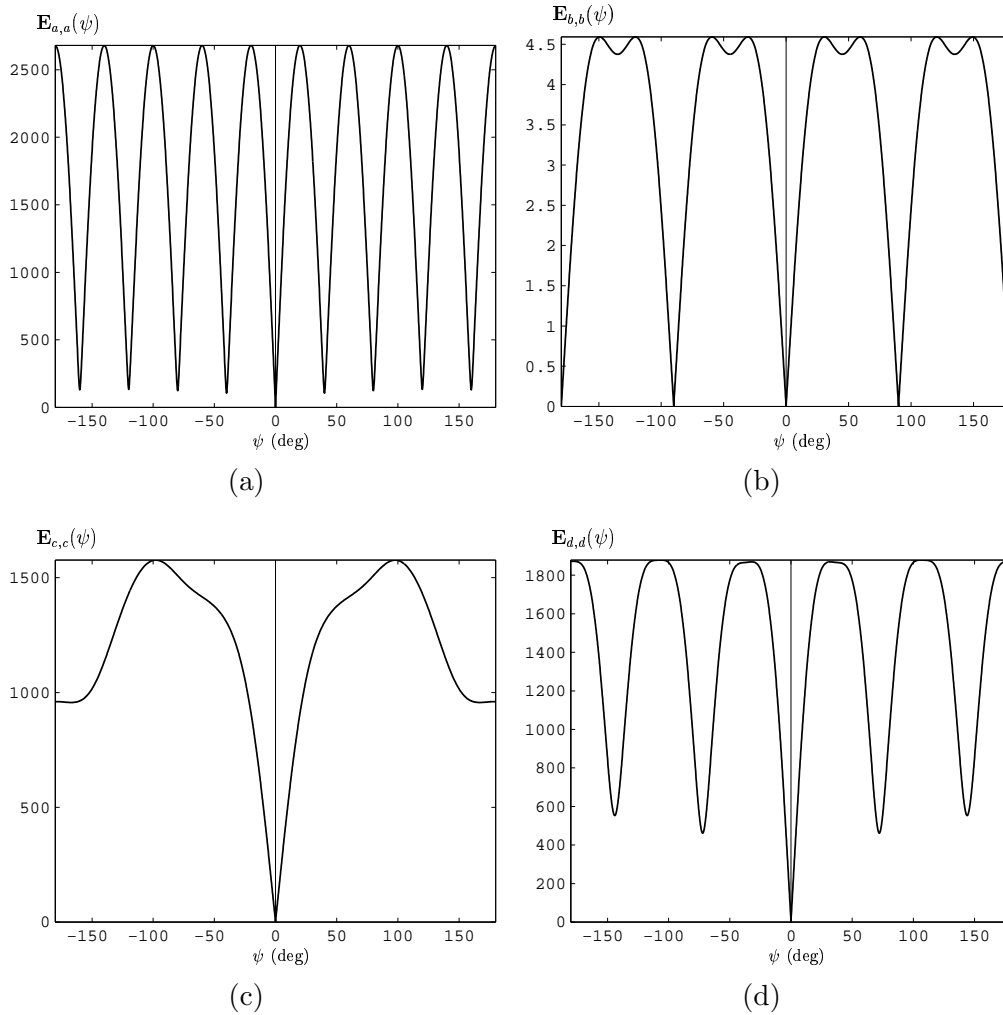


Fig. 10. Plot of $\mathbf{E}_{f_{\sigma}, f_{\sigma}}(\psi)$ for the four images in Fig. 8.

number” of folds.

For the detection and estimation of folds in an RSI f , we propose to compute $\mathbf{E}_{f_{\sigma}, f_{\sigma}}(\psi)$ from (12), which can be written as:

$$\forall \psi \in \mathbb{S}^1, \quad \mathbf{E}_{f_{\sigma}, f_{\sigma}}(\psi) = \left(2 \sum_{k \in \mathbb{Z}} (1 - \cos(k\psi)) \int_{-\infty}^{+\infty} |\mathcal{M}_{f_{\sigma}}(k, v)|^2 dv \right)^{\frac{1}{2}}. \quad (15)$$

It is easy to show that $\mathbf{E}_{f_{\sigma}, f_{\sigma}}$ is even and periodic with period $\frac{2\pi}{P}$. The orientation of the folds is given by angles ψ_i such that $\mathbf{E}_{f_{\sigma}, f_{\sigma}}(\psi_i) = 0$. The solution $\mathbf{E}_{f_{\sigma}, f_{\sigma}}(0) = 0$ is always true since any image is rotationally symmetric with respect to 0° rotation.

The detected axes for the shapes sketched in figure 8 are reported in figure 10. Angles are given from the x -axis and clockwise. The top-left result shows nearly zero values according to the fold axes of image 8(a). The min-

ima of the bottom-right result correspond to the rotation symmetric axes of the starfish (-144° , -72° , 0° , 72° , and 144°). For the disk image (top-right result), \mathbf{E} should have been exactly zero everywhere, which is not the case, due to approximations. We only get exactly zero for angles that are multiples of 90° since the Cartesian grid is isotropic to these angles (every pixel finds an exact location on the grid). Nevertheless, the curve is near zero compared to other results. The butterfly image is not rotationally symmetric and the only zero in the bottom left result is located at $\psi = 0$.

4.2 Reflection symmetric images

Two images f and g are called reflection-symmetric, if they are similar up to a reflection with respect to one line, denoted as the reflection-symmetric axis:

$$\forall (r, \theta) \in \mathbb{R}_+^* \times \mathbb{S}^1, \quad f(r, \phi + \theta) = g(r, \phi - \theta), \quad (16)$$

where ϕ is the angle between the x -axis and the symmetric axis. One can easily show that the AFMT harmonics of f and g are related according to :

$$\forall (k, v) \in \mathbb{Z} \times \mathbb{R}, \quad \mathcal{M}_{g_\sigma}(k, v) = e^{-2ik\phi} \mathcal{M}_{f_\sigma}(-k, v). \quad (17)$$

Fourier-Mellin harmonics on both parts of the k -axis have the same magnitude and a phase shift with angle $-2k\phi$.

Following work done for rotationally symmetric images, the matching between f and itself is computed according to:

$$\forall \phi \in \mathbb{S}^1, \quad \mathbf{F}_{f_\sigma, f_\sigma}(\phi) = \left(\int_0^\infty \int_0^{2\pi} r^{2\sigma} |f(r, \phi + \theta) - f(r, \phi - \theta)|^2 d\theta \frac{dr}{r} \right)^{\frac{1}{2}}.$$

In the Fourier-Mellin domain and using Eq. (17), we finally get :

$$\mathbf{F}_{f_\sigma, f_\sigma}(\phi) = \left(\int_{-\infty}^{+\infty} \sum_{k \in \mathbb{Z}} \left| \mathcal{M}_{f_\sigma}(k, v) - e^{-2ik\phi} \mathcal{M}_{f_\sigma}(-k, v) \right|^2 dv \right)^{\frac{1}{2}}. \quad (18)$$

\mathbf{F} is zero for each angle ϕ which defines a reflection symmetric axis (angle $\phi + \pi$ denotes the same axis). It is easy to verify that $\mathbf{F}_{f_\sigma, f_\sigma}$ is also even and periodic according to two times the number of reflection axes. Due to approximations, the axes are estimated by searching for the minima in $\mathbf{F}_{f_\sigma, f_\sigma}$.

Fig. 11 reports the results obtained from the images in Fig. 8. Angles are given in degrees from the x -axis and clockwise. The range of ϕ is restricted to $[0^\circ; 180^\circ[$ due to the parity of \mathbf{F} . The plots clearly show minima located at the angles of the symmetric axes of the images. Each image shows either one (the

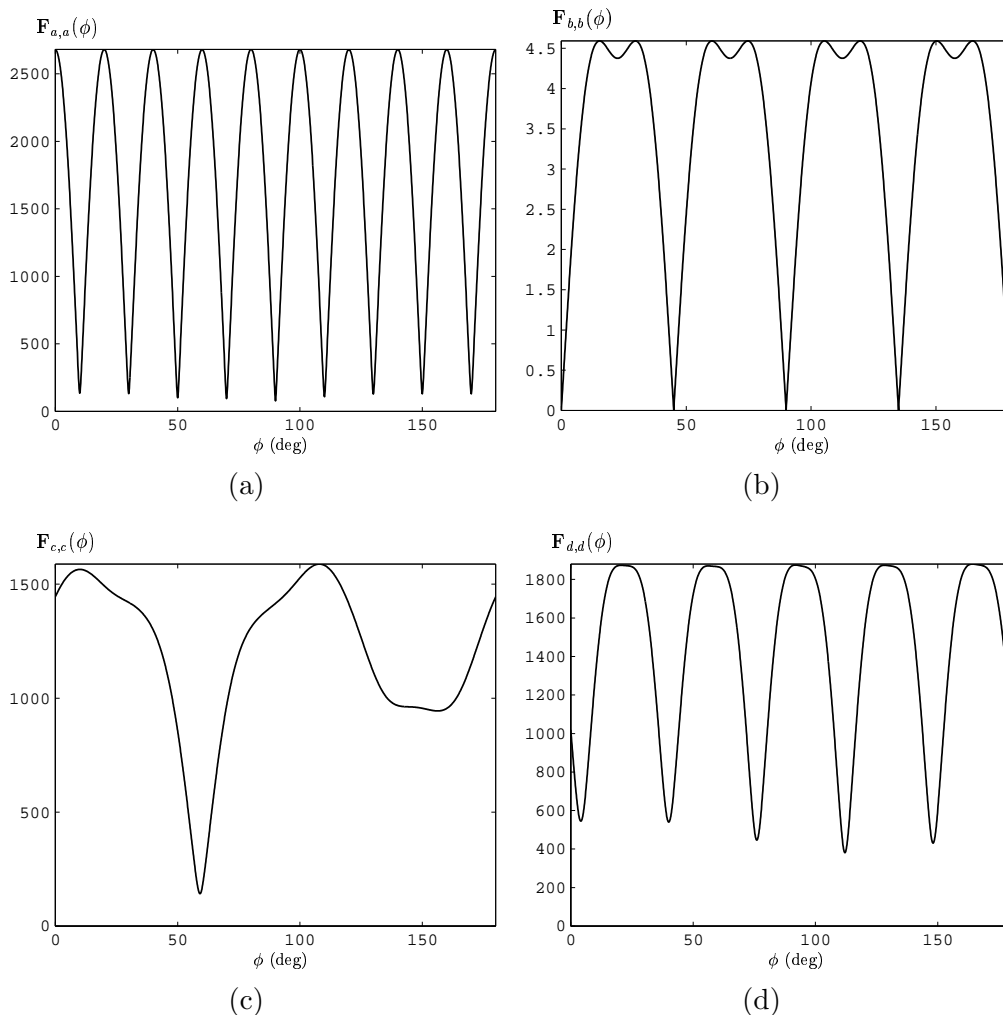


Fig. 11. Plot of $\mathbf{F}_{f_{\sigma}, f_{\sigma}}(\phi)$ for the four images in Fig. 8.

(c) image), or N symmetric axes (the other three images) with N the number of rotational symmetries in the image.

4.3 Further experiments and discussion

The aim of this section is, first, to give the reader an idea on the reliability of the symmetry detection algorithms and, second, to discuss the intrinsic limitations of the method. All the experiments are conducted on the aerial images of roundabouts in Fig. 12. These images show complex and noisy shapes and allow to test the algorithms to non perfect symmetry, rough segmentation and small perspective transformations due to the viewpoint. All the results reported here come from the reflection symmetry detection algorithm.

The FMT is a global transform and applies on all pixels in the same way. Hence, the detection algorithms are not appropriated to handle objects lost

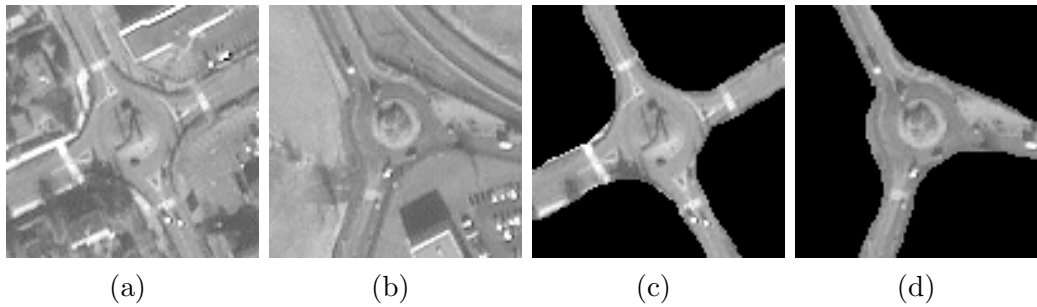


Fig. 12. Images (a) and (b) show two aerial pictures of roundabouts (panchromatic Ikonos image, ground resolution: 1 meter), by courtesy of CNES. Images (c) and (d) show the roundabout after extraction from the background.

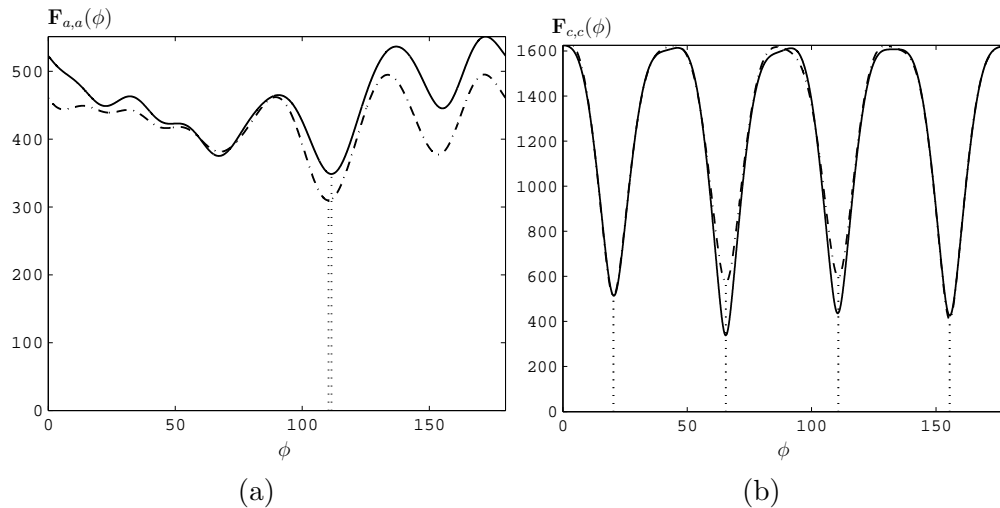


Fig. 13. Plot of $\mathbf{F}(\phi)$ for the (a) and (c) images in Fig. 12. The dashed curves were obtained when the center of coordinates was set automatically to the center of gravity whereas the plain curves were obtained when the center of coordinates was set manually.

in a complex background, i.e. without a prior extraction from the scene they belong to. Indeed, all the symmetry axes of an object necessarily intersect each other at the center of gravity. In the case of a scene with a complex background, the center of gravity can be far from the one obtained with the isolated object and detecting symmetry axes becomes impossible. This remark is illustrated in Fig. 13(a), where some of the minima are difficult to localize. It is clear that the symmetry axes can be detected reliably only when the roundabout has been previously extracted from the scene (Fig. 13(b)). In that case, we obtained the four following angles: 20.4° , 65.6° , 110.8° and 155.5° . The same experiment was conducted on the (d) image in Fig. 12 and we obtained the three following angles: 55.5° , 116.9° and 172.8° . Fig. 14 shows the superposition of the estimated axes with the original images.

To conclude with these experiments, we may say that the symmetry detection algorithms can deal with small local deformations and occlusions of shapes,

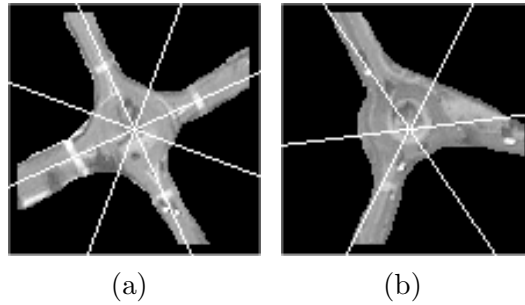


Fig. 14. Superposition of the estimated reflection axes with the images.

under the assumption that objects have been previously extracted from the scene. As mentioned, a good localization of the center of coordinates is an important issue to obtain reliable estimations.

5 Conclusion

In this paper, we considered the problem of estimating the scale and orientation differences between gray-level objects. This problem has been formulated as the minimization of a functional defined from the Analytical Fourier-Mellin Transform representation of objects. This functional was constructed according to an appropriate Euclidean distance involving the rotation and scale parameters of the similarity group. It has also been shown to be useful for the evaluation of global shape difference between objects since its minimum also furnishes a measure of similarity between objects.

We also investigated the problem of estimating rotational and reflectional symmetries in objects. We have shown that, when only the group of rotations is considered, the shape space is metric and its natural distance is the Hausdorff one expressed in the Fourier-Mellin domain. This result ensures the uniqueness of parameters and extends the result obtained in [20] for planar closed contours and Fourier coefficients to gray-level images and AFMT. As an application, we proposed two algorithms in order to detect and localize all the rotational and reflectional symmetry axes of any gray-level object. One advantage is that we do not assume the images to be symmetric since the values of the minima can be used to determine whether the input image is symmetric or not. The experiments conducted on two noisy and non perfect symmetric aerial pictures of roundabouts seem to confirm the reliability of the method and the robustness of the algorithms.

Acknowledgments The authors are grateful to the Remote Sensing Image Processing Division, CNES, French Space Agency for providing the Ikonos images of roundabouts.

References

- [1] Y. Sheng and H.H. Arsenault. Experiments on pattern recognition using invariant Fourier-Mellin descriptors. *J. of the Optical Society of America A*, 3(6):771–776, June 1986.
- [2] A.E. Grace and M. Spann. A comparison between Fourier-Mellin descriptors and moment based features for invariant object recognition using neural networks. *Pattern Recognition Letters*, 12:635–643, October 1991.
- [3] R. Milanese and M. Cherbuliez. A rotation-, translation-, and scale-invariant approach to content-based image retrieval. *J. of Visual Communication and Image Representation*, 10:186–196, June 1999.
- [4] P.E. Zwicke and Z. Kiss. A new implementation of the Mellin transform and its application to radar classification. *IEEE trans. on Pattern Analysis and Machine Intelligence*, 5(2):191–199, March 1983.
- [5] F. Ghorbel. A complete invariant description for gray-level images by the harmonic analysis approach. *Pattern Recognition Letters*, 15:1043–1051, October 1994.
- [6] S. Derrode and F. Ghorbel. Robust and efficient Fourier-Mellin transform approximations for gray-level image reconstruction and complete invariant description. *Computer Vision and Image Understanding*, 83(1):57–78, July 2001.
- [7] F. Ghorbel. Towards a unitary formulation for invariant image description; Application to image coding. *Annals of Telecommunications*, 53(3):143–153, May 1998.
- [8] I. Rothe, K. Voss, and H. Suesse. The method of normalization to determine invariants. *IEEE trans. on Pattern Analysis and Machine Intelligence*, 18(4):366–375, April 1996.
- [9] D.P. Huttenlocher and S. Ullman. Recognizing solid objects by alignment with an image. *Int. J. of Computer Vision*, 5(2):195–212, 1990.
- [10] Q. Chen, M. Defrise, and F. Deconinck. Symmetric phase-only matched filtering of Fourier-Mellin transforms for image registration and recognition. *IEEE trans. on Pattern Analysis and Machine Intelligence*, 16(12):1156–1168, 1994.
- [11] T.M. Lehmann. A two-stage algorithm for model-based registration of medical images. In *Proc. of the 4th Int. Conf. on Pattern Recognition*, volume 1, pages 344–351, 1998.
- [12] L. Benyoussef, Y. Delignon, and F. Ghorbel. An optimal matched filter for target detection in images distorted by noise. In *Proc. of the Int. Conf. on Geoscience and Remote Sensing*, volume 2, pages 1001–1003, Seattle (USA), 6–10 July 1998.
- [13] D. Shen, H.H.S. Ip, and E.K. Teoh. An energy of asymmetry for accurate detection of global reflection axes. *Image and Vision Computing*, 19:283–297, 2001.
- [14] R. Lenz. *Group theoretical methods in image processing*, volume 413 of *Lecture notes in computer science*. Springer-Verlag, Berlin, Germany, G.

- Goos and J. Hartmanis edition, 1990.
- [15] J. Turski. Projective Fourier analysis for patterns. *Pattern Recognition*, 33:2033–2043, 2000.
 - [16] J. Dieudonné. *Éléments d'analyse*. Tome II. Gauthier-Villars, Cahiers scientifiques, Paris (Fr.), third edition, 1983.
 - [17] W. Rudin. *Fourier analysis on groups*. Wiley Classics, New York, 1990.
 - [18] M. Pavel. *Fundamentals of pattern recognition*. Pure and applied mathematics. Marcel Dekker, Inc., New York, 1989.
 - [19] M. Hagedoorn and R.C. Veltkamp. Reliable and efficient pattern matching using an affine invariant metric. *Int. J. of Computer Vision*, 31(2/3):203–225, April 1999.
 - [20] M. Daoudi, F. Ghorbel, A. Mokadem, O. Avaro, and H. Sanson. Shape distances for contour tracking and motion estimation. *Pattern Recognition*, 32:1297–1306, June 1999.
 - [21] R. Lenz. Describing and recognizing group-invariant pattern classes with group-sampling. *Pattern Recognition Letters*, 9:169–173, April 1989.
 - [22] J.L. De Bougrenet de la Tocnaye and F. Ghorbel. Scale-rotation invariant pattern recognition applied to image data compression. *Pattern Recognition Letters*, 8:55–58, July 1988.
 - [23] G. Tzanetakis, M. Traka, and G. Tziritas. Motion estimation based on affine moment invariants. In *IX European Signal Processing Conference (Eusipco98)*, volume 2, pages 925–929, Island of Rhodes (Greece), September 8-11 1998.
 - [24] W.H. Press, S.A. Teukolsky, A.T. Vetterling, and B.P. Flannery. *Numerical recipes in C, the art of scientific computing*. Cambridge university press, second edition, 1983.
 - [25] D.P. Huttenlocher, G.A. Klanderman, and W.J. Rucklidge. Comparing images using the Hausdorff distance. *IEEE trans. on Pattern Analysis and Machine Intelligence*, 15(9):850–863, September 1993.
 - [26] W.J. Rucklidge. *Efficient visual recognition using the Hausdorff distance*, volume 1173 of *Lecture notes in computer science*. Springer-Verlag, Berlin, Germany, 1996.
 - [27] X. Yi and O.I. Camps. Line feature based recognition using Hausdorff distance. In *Proc. of the first Int. Symp. on Computer Vision*, pages 79–84, Coral Gables (Fl.), November 1995.
 - [28] D. Shen, H.H.S. Ip, K.K.T. Cheung, and E.K. Teoh. Symmetry detection by generalized complex (GC) moments: A close-form solution. *IEEE trans. on Pattern Analysis and Machine Intelligence*, 21(5):466–475, May 1999.

Biographical sketches

Stéphane DERRODE received the telecommunication engineering degree from Télécom Lille I, France in 1995, and the Ph.D. degree from the University of Rennes, France, in 1999. Since 2001, he has been with the *École Nationale Supérieure de Physique de Marseille*, France, where he is currently an Associate Professor in the multidimensional signal processing group, Fresnel Institute. His research interests include, on the first hand, group theoretical image representation and geometrical invariance for pattern recognition and content-based image indexing, and, on the other hand, hidden Markov models and parameters estimation for remote sensing image classification.

Faouzi GHORBEL received the telecommunication engineering and PhD degrees both from the *École Nationale Supérieure des Télécommunications de Bretagne*, France, in 1987 and 1990 respectively. From 1990 to 1997, he was head of the pattern recognition group at the ENIC and received the *Habilitation à Diriger des Recherches* from the University of Rennes I, France, in 1995. He is currently professor at the University of Tunis II and the head of the *Groupe de Recherche Image et Formes de Tunisie, laboratoire Cristal*. He is co-chair of the TAIMA workshop (*Traitement et Analyse de l'Information: Méthodes et Applications*) organized every two years in Hammamet (Tunisia). His main research areas include group theory and harmonic analysis in image processing, invariance and pattern recognition for medical imaging and multimedia applications.

List of Figures

- 1 Direct and inverse AFMT approximations (fast algorithm, $\sigma = 0.5$). (a) Original image. (b) Magnitude of central Fourier-Mellin harmonics. (c) Reconstructed version from a finite and discrete Fourier-Mellin spectrum. 5
- 2 Three images of a butterfly used for the illustration of algorithms. Images (a) and (b) represent the same butterfly with distinct positions ($\alpha = 0.75$ and $\beta = 60^\circ$). The (b) picture has been artificially computed from the (a) one. Image (c) is a butterfly with a distinct shape. 8
- 3 Illustration of the elementary algorithm using images (a) and (b) in Fig. 2. The cross symbol denotes the real parameters ($\alpha = 0.75$, $\beta = 1$ rad) whereas a diamond shows an estimate. 9
- 4 Three-dimensional plots of \mathbf{E} for (a) the similar images, and (b) the distinct images in Fig. 2. Figure (b) clearly shows no prevailing minimum. 10
- 5 Zoom on the pit in figure 4(a). The path through the surface shows the five optimization steps from the initial estimation $(\hat{\rho}_0, \hat{\psi}_0)$ to the final estimation $(\hat{\rho}_{\mathbf{E}}, \hat{\psi}_{\mathbf{E}})$ (cf. Table 1). The threshold has been set to 10^{-5} . 12
- 6 Two still pictures of an electronic board acquired with a digital camera. The (c) image represents the three-dimensional plot of \mathbf{E} and exhibits a minimum that corresponds to the estimated scale and rotation parameters between (a) and (b). 13
- 7 Plot of the Hausdorff distance (b) computed from the two images in (a). The second picture has been artificially computed from the first one. The minimum value $\Delta = 23.61$ is attained for $\psi = 35.02^\circ$. 15
- 8 Four test images used for symmetry detection and estimation experiments. (a) and (b) are binary images whereas (c) and (d) are gray-level ones. 15
- 9 Magnitude of central Fourier-Mellin harmonics of the images (a), (d) and (b) in Fig. 8, respectively. 16
- 10 Plot of $\mathbf{E}_{f_\sigma, f_\sigma}(\psi)$ for the four images in Fig. 8. 17

11	Plot of $\mathbf{F}_{f_\sigma, f_\sigma}(\phi)$ for the four images in Fig. 8.	19
12	Images (a) and (b) show two aerial pictures of roundabouts (panchromatic Ikonos image, ground resolution: 1 meter), by courtesy of CNES. Images (c) and (d) show the roundabout after extraction from the background.	20
13	Plot of $\mathbf{F}(\phi)$ for the (a) and (c) images in Fig. 12. The dashed curves were obtained when the center of coordinates was set automatically to the center of gravity whereas the plain curves were obtained when the center of coordinates was set manually.	20
14	Superposition of the estimated reflection axes with the images.	21

List of Tables

1	Optimization steps for images (a) and (b) in Fig. 2.	12
---	--	----